Mechanisms of Stress- and Fluid-Pressure-Driven Fault Reactivation in Gonghe Granite: Implications for Injection-induced Earthquakes

Chongyuan Zhang[1], Dongjue Fan[2], Derek Elsworth[3], Xingguang Zhao[4], Chun Zhu[5], Man-chao He[6], and Hao Zhang[1]

[1]Institute of Geomechanics, Chinese Academy of Geological Sciences
[2]University of Science and Technology Beijing
[3]Pennsylvania State University
[4]Beijing Research Institute of Uranium Geology
[5]School of Earth Sciences and Engineering
[6]China University of Mining and Technology (Beijing)

December 3, 2023

Abstract

We explore the impacts of stress- and fluid-pressure-driven frictional slip on variably roughened faults in Gonghe granite (Qinghai Province, China). Slip is on an inclined fault under simple triaxial stresses with concurrent fluid throughflow allowing fault permeability to be measured both pre- and post-reactivation. Under stress-drive, smooth faults are first slip-weakening and transition to slip-strengthening with rough faults slip-strengthening, alone. A friction criterion accommodating a change in friction coefficient and fault angle is able to fit the data of stable-slip and stick-slip. Under fluid-pressure-drive, excess pore pressures must be significantly larger than average pore pressures suggested by the stress-drive-derived failure criterion. This overpressure is conditioned by the heterogeneity of the pore pressure distribution in radial flow on the fault and related to the change in permeability. Fault roughness impacts both the coefficient of friction and the permeability and therefore exerts important controls in fluid-injection-induced earthquakes. The results potentially improve our ability to assess and mitigate the risk of injection-induced earthquakes in EGS.

Hosted file

`961828_0_art_file_10925003_rtm38d.docx` available at https://authorea.com/users/610972/articles/639716-mechanisms-of-stress-and-fluid-pressure-driven-fault-reactivation-in-gonghe-granite-implications-for-injection-induced-earthquakes

Hosted file

`961828_0_supp_10924920_rtm2b8.docx` available at https://authorea.com/users/610972/articles/639716-mechanisms-of-stress-and-fluid-pressure-driven-fault-reactivation-in-gonghe-granite-implications-for-injection-induced-earthquakes

Hosted file

`961828_0_author_info_file_10925600_rtmxc0.docx` available at https://authorea.com/users/610972/articles/639716-mechanisms-of-stress-and-fluid-pressure-driven-fault-reactivation-in-gonghe-granite-implications-for-injection-induced-earthquakes

Mechanisms of Stress- and Fluid-Pressure-Driven Fault Reactivation in Gonghe Granite: Implications for Injection-induced Earthquakes

Chongyuan Zhang[1, 2], Dongjue Fan[1, 3], Derek Elsworth[4], Xingguang Zhao[5], Chun Zhu[6], Manchao He[2], Hao Zhang[1]

[1] Institute of Geomechanics, Chinese Academy of Geological Sciences, Beijing, 100081, China

[2] School of Mechanics and Civil Engineering, China University of Mining and Technology, Beijing 100083, China

[3] School of Civil and Resource Engineering, University of Science and Technology Beijing, Beijing, 100081, China

[4] Energy and Mineral Engineering, EMS Energy Institute and G3 Center, Pennsylvania State University, University Park, 16802, USA

[5] CNNC Key Laboratory on Geological Disposal of High-level Radioactive Waste, Beijing Research Institute of Uranium Geology, Beijing 100029, China

[6] School of Earth Sciences and Engineering, Hohai University, Nanjing, 210098, China

Corresponding author: Chongyuan Zhang (zhchongyuan@126.com, zhangchy@cags.ac.cn)

Key Points:

- The mechanism of fault slip in stress- and fluid-pressure-driven frictional slip experiments on granite faults is demonstrated

- By modifying the slip weakening criterion, a slip friction criterion considering friction strengthening and fault angle is established

- Fault activation mechanism and the influence of fault permeability on fracture overpressure during fluid injection have been studied

Abstract

We explore the impacts of stress- and fluid-pressure-driven frictional slip on variably roughened faults in Gonghe granite (Qinghai Province, China). Slip is on an inclined fault under simple triaxial stresses with concurrent fluid throughflow allowing fault permeability to be measured both pre- and post-reactivation. Under stress-drive, smooth faults are first slip-weakening and transition to slip-strengthening with rough faults slip-strengthening, alone. A friction criterion accommodating a change in friction coefficient and fault angle is able to fit the data of stable-slip and stick-slip. Under fluid-pressure-drive, excess pore pressures must be significantly larger than average pore pressures suggested by the stress-drive-derived failure criterion. This overpressure is conditioned by the heterogeneity of the pore pressure distribution in radial flow on the fault and related to the change in permeability. Fault roughness impacts both the coefficient of friction and the permeability and therefore exerts important controls in fluid-injection-induced earthquakes. The results potentially improve our ability to assess and mitigate the risk of injection-induced earthquakes in EGS.

Plain Language Summary

Enhanced geothermal systems (EGS) inject large amounts of fluid into a rock mass, leading to the slip of faults in the strata and thus causing earthquakes. Unlike the US and European EGS, many geothermal fields are located in seismically active areas with high tectonic stress levels in Western China, such as the Gonghe EGS. However, the mechanism of injection-induced seismicity under a high tectonic stress is still unclear. Herein, we report the results obtained from frictional slip tests under stress- and fluid-pressure-driven conditions in granite faults. Our results show that the slip form of the fault is determined by its roughness. Under stress-driven condition, a rougher fault slips more stably, while a smoother fault shows a sudden and rapid slip. During fluid injection, all the faults with different roughnesses showed stick-slip phenomenon. Obviously, the mechanisms of fault instability in the two methods are substantially different. In addition, the uneven distribution characteristic of pore pressure depending on permeability differences resulted in a higher pore pressure required for fault instability than the predicted pore pressure by Mohr-Coulomb criterion. This study revealed the mechanisms of stress- and fluid-pressure-driven fault reactivation, and explain the influence of roughness and permeability of faults on injection-induced earthquakes.

1 Introduction

Fluid injection is a preferred method for the stimulation of Enhanced Geothermal Systems (EGS) to elevate permeability from micro- to milli-Darcy levels. Fluid injection-induced reductions in effective stress are capable of reactivating fractures in brittle failure. The key is to generate permeability through shear reactivation but avoid creating runaway slip that can trigger large seismic events (Lengliné et al., 2017). Since 2019, China has initiated its first EGS development project in the Gonghe basin on the northeastern extent of the Tibetan plateau (Zhang et al., 2022). The northeastern part of the Qinghai–Tibet Plateau is a tectonically active area with a high risk of strong earthquakes. In 1990, an Mw 6.4 earthquake occurred ~30 km from the Gonghe EGS site (Hao et al., 2012). The Gonghe EGS is in a still higher stress environment with a further elevated risk of injection-induced seismicity. Controls on fluid injection induced seismicity on variable roughness faults under non-stationary and strongly heterogeneous distributions of pore fluid pressures remain unclear. To address this issue, we complete experiments and analytical characterizations on laboratory faults under various total stress and fluid pressure stress paths.

Characterizations of fault friction based on constant friction (Jaeger et al., 2009) are unable to replicate stick-slip phenomena observed during earthquakes. Rate- or velocity-weakening response is a necessary requirement (Scholz et al., 1972; Dieterich, 1978) to replicate this behavior. Slip weakening may be defined over a slip weakening distance (Palmer and Rice, 1973) and as a function of state (Dieterich, 1979). These relations usually define the evolution of second-order frictional effects under prescribed velocity conditions and under constant effective stress - but stress paths are rarely simple and fluid injection reactivations can be strongly varying in both space and time.

Injection-induced earthquakes are impacted by the minimum principal stress (Maurer & Segall, 2018), the total volume of injected fluid (Galis et al., 2017) or related to Gutenberg-Richard statistics (van der Elst et al., 2016; Yu et al., 2022). These models assume that pore pressure is uniformly distributed during fluid injection, but laboratory tests and field studies show that the fluid pressure required to activate a fault is often higher than that predicted using the Mohr–Coulomb failure criterion. An uneven diffusion of fault overpressure substantially affects the stress field and fault stability. The overpressure distribution (Ji et al., 2020, 2021), together with the heterogeneous diffusion of pore pressure (Passelègue et al.,2018; Ishibashi et al., 2018; Wang et al., 2020) impact fault instability driven by injection. During the injection, the distribution of pore

92   pressure in a fault is influenced by various factors such as fault roughness, in-situ stress state,

93   mineral composition, and injection conditions (Fang & Wu, 2022). These factors are implicit in

94   defining the heterogeneous permeability of faults and thereby the uneven distribution of pore
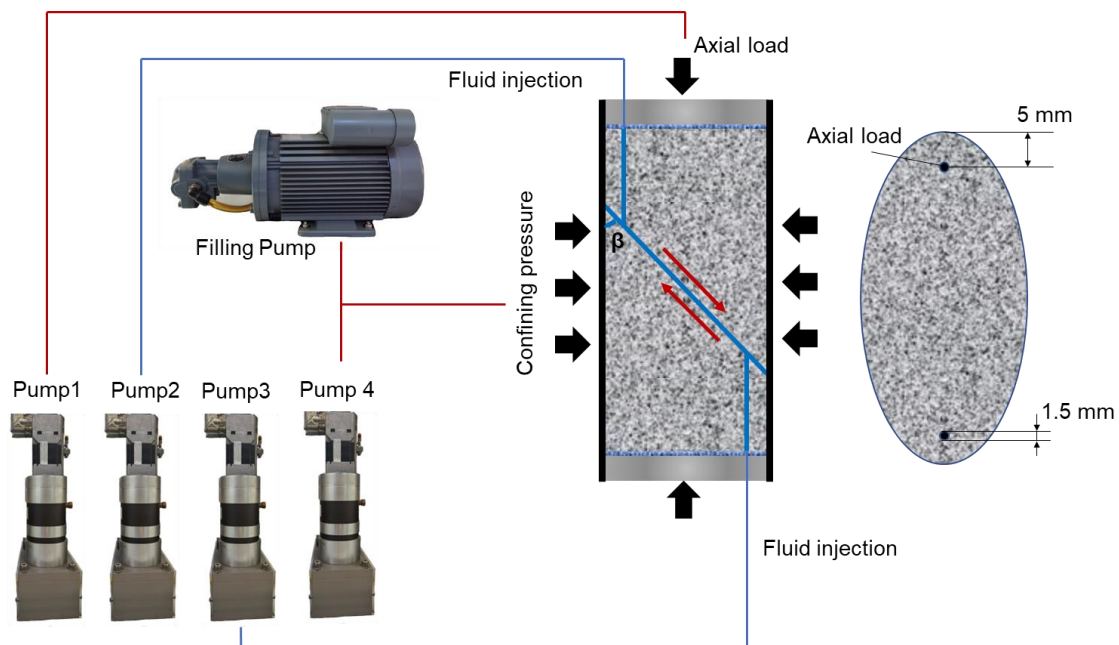
95   pressure.

96   At present, several experimental methods have been developed to simulate the frictional slip on

97   rock faults. According to the characteristics of loading, they can be divided into single direct shear,

98   double direct shear, rotary shear, and triaxial shear testing configurations. Single direct shearing is

99   conducted by fixing the lower fault and applying normal and shear loads to the upper block (Zhao

100   et al., 2018a, b). This method has simple stress boundary conditions, but the load distribution on

101   the fault surface is not uniform due to its loading characteristics. Double direct shearing uses three

102   blocks with two parallel fault interfaces to apply a near uniform and moment-free shear stress to

103   two fault surfaces (Collettini, 2014). This enables a more uniform distribution of shear load on the

104   fault surface. Under rotary shear (Ujiie & Tsutsumi, 2010; Cornelio et al., 2019), the shear stress

105   is applied by fixing the upper/lower part of a toroidal rock sample and rotating the lower/upper

106   part around a central axis under applied normal stress. This method can represent both high shear

107   rates and large shear displacements. However, rotary shear has difficulty in applying large excess

108   pore pressures to the fault. Triaxial shear tests allow inclined faults traversing a cylindrical sample

109   to be reactivated (Wu et al., 2017; Ye & Ghassemi, 2018). Cylindrical rock samples containing 45°

110   to 60° prefabricated fractures are used to concurrently apply normal and shear stress to the

111   laboratory fault *via* confining pressure and axial stress. Triaxial shear tests allow control of the

112   ratio of normal to shear stress through the selection of fault angle as a complex stress together with

113   the ready application of temperature and pore pressures.

114   To address the mechanism of stress- and fluid-pressure-driven instability of various roughness

115   faults we complete experiments and analytical characterizations on laboratory faults under various

116   total stress and fluid pressure stress paths. The mechanical (stress and displacement) and transport

117   characteristics (pore pressure and permeability) of faults with different surface roughness were

118   characterized to constrain frictional slip under both total stress- and fluid-pressure-driven stress

119   paths. Finally, we discuss the effect of fault roughness and permeability on injection-induced

120   earthquakes to improve our ability to assess and mitigate the risk of anthropogenic earthquakes in

121   EGS.

2 Materials and Methods

The granites used in this study are surface outcrop derived samples of granites from the Gonghe basin, Qinghai Province, China. These granites are 37% quartz, 33% microplagioclase, 25% mica, 3% amphibole, and 2% plagioclase (Chen et al., 2020) by volume. The resulting cylindrical samples are 50 mm in diameter and 100 mm in height and contain a diamond sawcut fault inclined at 45° and pierced by two 1.5-mm-diameter boreholes accessing pressurized fluids from the end platens. The boreholes were used to change pressures and therefore effective stresses and also to measure permeability before and after slip. The fault surfaces are roughened with sandpaper corresponding to particle sizes of 150 μm, 23 μm, and 1.3 μm, for different fault roughnesses. A Top Industrie high-temperature triaxial testing system was used to conduct the reactivation experiments. The maximum axial load of the system is 1500 kN with confining pressures and pore pressures in the range 0–60 MPa. Silicon oil is used as the confining fluid. The sample and test configuration are shown in Figure 1.

Nine rock samples were produced from the same surface outcrop sample with the cylindrical samples divided into three groups according to the variable roughnesses of the fault surfaces. Sample information is shown in Table 1.

Figure 1. Schematic of rock sample and testing configuration. Four pumps separately regulate the axial pressure, confining pressure and the pore pressure at both ends of the sample.

142 Each test consists of two separate stress paths: stress-driven frictional slip followed by fluid-
143 pressure-driven frictional slip. Specific test procedures are described as follows:

144 **Step 1: Initial state.** The sample was vacuum saturated with deionized water and then sealed by
145   polyurethane sleeves before hydrostatic loading ($\sigma_1 = \sigma_2 = \sigma_3$). Previous research has shown
146   that the friction coefficients of fault in rock decrease as a result of pore water presence
147   (Byerlee, 1967). In order to ensure that the fault is always saturated during the test, a pore
148   pressure of 1 MPa was then applied to saturate the fault before being reduced to 0.5 MPa.
149   Fault permeability was measured for steady state flow (Brace et al., 1968) with an upstream
150   (1.5 MPa) to downstream (0.5 MPa) pore pressure differential of 1 MPa.

151 **Step 2: Stress-driven fault activation**. We selected constant stress as a load target in order to
152   ensure that faults with different roughness are at the same stress level before injection.
153   Axial stress targets were larger than the reactivation stress of the fault and increased with
154   the confining pressure. Axial stress was applied at 0.01 MPa/s according to the
155   experimental schedule of Table 1. This results in normal and shear stresses increasing
156   simultaneously on the fault with the rate of shear stress increase greater than that of the
157   normal stress. When the shear stress exceeds the maximum frictional strength the fault, the
158   fault slips and the static frictional strength was recorded to calculate the coefficient of
159   friction. Subsequently, the fault went through the initial run-in stage until the axial stress
160   retained constant. Fault permeability was measured using the method of Step 1.

161 **Step 3: Fluid-pressure-driven fault reactivation.** Deionized water was injected into both
162   boreholes simultaneously at a rate of 0.05 cm^3/min after the fault reached steady state. The
163   increase in pore pressure leads to a decrease in effective normal stress and the reactivation
164   of fault slip – that reactivation pore pressure is recorded. The pore pressure continues to
165   increase to 50% of the confining pressure after reactivation. Then, the outlet pore pressure
166   was retained constant and the inlet pore pressure increased by 1 MPa with the fault
167   permeability measured as above.

168 The axial force applied to the sample is usually measured using a load cell located outside the
169 pressure vessel. In this case, however, part of the measured force is resisted by the friction between
170 the moving piston and the confining sealing assembly (Tembe et.al, 2010). Therefore, a load cell
171 was located inside the confining pressure vessel to measure true axial force applied to the sample.

172   The axial force was also corrected by considering and calibrating out jacket restraint during the

173   tests (Ji, 2020).

174   The axial displacement (Δl) can be obtained from a linear variable displacement transducer (LVDT)

175   installed on the sample. The fault slip displacement (u) can therefore be estimated as,

176
$$u = (\Delta l - \frac{\sigma_1 \cdot l}{E}) \cdot \frac{1}{\cos \beta} \tag{1}$$

177   where β is the dip angle of the fault surface (in our case, β=45°), E is the Young's modulus of the

178   granite, σ_1 is axial stress and l is the length of the cylindrical sample. In this study, axial stress σ_1

179   is computed by dividing the uncorrected stress by the factor A/A_0,

180
$$A / A_0 = (\theta - \sin \theta) / \pi \tag{2}$$

181
$$\theta = \pi - 2\sin^{-1}\left[(u / dr)\tan \beta\right] \tag{3}$$

182   where θ is the angle subtended by the points of intersection of two overlapping circles. At the

183   centers of the circles, A_0 and A are the original and corrected cross-sectional areas of the sample.

184   In this study, the maximum fault shear displacement does not exceed 2mm, and the area correction

185   results in a stress adjustment of 3.59% at 2mm.

186   The normal stress and shear stress on the fault surface in the center of the sample were calculated

187   from the axial stress σ_1 and confining pressure σ_3 as:

188
$$\tau = \frac{1}{2}(\sigma_1 - \sigma_3)\sin 2\beta = (\sigma_1 - \sigma_3)\sin \beta \cos \beta \tag{4}$$

189
$$\sigma_n = \frac{1}{2}\left[(\sigma_1 + \sigma_3) - (\sigma_1 + \sigma_3)\cos 2\beta\right] = \sigma_3 + (\sigma_1 - \sigma_3)\sin^2 \beta \tag{5}$$

190   The aperture used to calculate permeability was determined from the cubic law.

191
$$Q = \frac{g}{v}\frac{we^3}{12}J \tag{6}$$

192   where Q is the volumetric flow rate within the fracture, w is the width of the cross-sectional area

193   of flow between parallel plates, v is the kinematic viscosity of the fluid, g is the gravitational

194   acceleration and J is the hydraulic gradient of unity. By measuring the flow rate of the fault, the

195   equivalent hydraulic aperture e_h can be determined. Combined with Darcy's law, the permeability

196   k of the fracture can be obtained from

197
$$k = \frac{e_h{}^2}{12} \qquad (7)$$

198   All data are acquired in real-time at a sampling rate of 10 Hz with fault roughness measured by a

199   3D laser scanner both pre- and post-test to define evolving damage characteristics of the fault

200   surface during the reactivation.

201   **Table 1.** Rock sample characteristics and experiment matrix.

Sample Number	Size of sandpaper (μm)	Confining pressure (MPa)	Axial stress (MPa)	Load rate (MPa/s)	Injection rate (mL/s)
1-1	150	10	34	0.01	0.05
1-2	150	20	68	0.01	0.05
1-3	150	40	136	0.01	0.05
2-1	23	10	34	0.01	0.05
2-2	23	20	68	0.01	0.05
2-3	23	40	136	0.01	0.05
3-1	1.3	10	34	0.01	0.05
3-2	1.3	20	68	0.01	0.05
3-3	1.3	40	136	0.01	0.05

202   **3 Experimental Result**

203   3.1 Fault slip characteristics

204   The shear stress on the fault is normally obtained by a displacement-driven shear test which is

205   carried out at an axial displacement rate (Ji & Wu, 2020). However, this method can only estimate

206   the shear stress of fault at steady state slip, without accurately estimating the slip point and the

207   change of friction coefficient in the initial run-in period under stress-drive. In order to obtain the

208   intact slip characteristics of the fault under stress-drive, we use a constant loading rate instead of

209   a constant displacement rate. Figures 2a-2c show the stress/pressure/displacement versus time

210   behavior under stress- and then fluid-pressure-driven reactivation (using a representative example

211   at a confining pressure of 20 MPa with all other results catalogued in the supporting information

212   S1). In stress-driven fault activation, the stable stage in which shear displacement does not increase

213   on a fault can be observed clearly. As the axial stress continues to increase, the fault slips at a

214   constant shear rate after an acceleration. At this time, the fault enters the steady-state initial

215   condition after the initial run-in period.

216   Subsequently, the faults with varied roughness showed different reactivation characteristics under

217   stress-driven conditions. For the roughest fault (roughened at 150 μm; Figure 2a), the fault

218   reactivated with stable-slip that arrested when the axial loading was stopped. For the medium-

219   roughness fault (roughened as 23 μm; Figure 2b) a small stress drop occurred after reactivation

220   before stable slip resumes. Finally, the smoothest fault (a particle size of 1.3 μm; Figure 2c)

221   reactivates in stick-slip with a large stress drop and shear displacement and accompanied by an

222   audible noise. Multiple stick-slips followed until the axial stress remained stable after the fault slip

223   stopped. In addition, the peak stress in rock sample 3-3 was limited by repeated stick-slip.

224   Therefore, a liquid injection-induced slip test was carried out while keeping the axial stress at 100
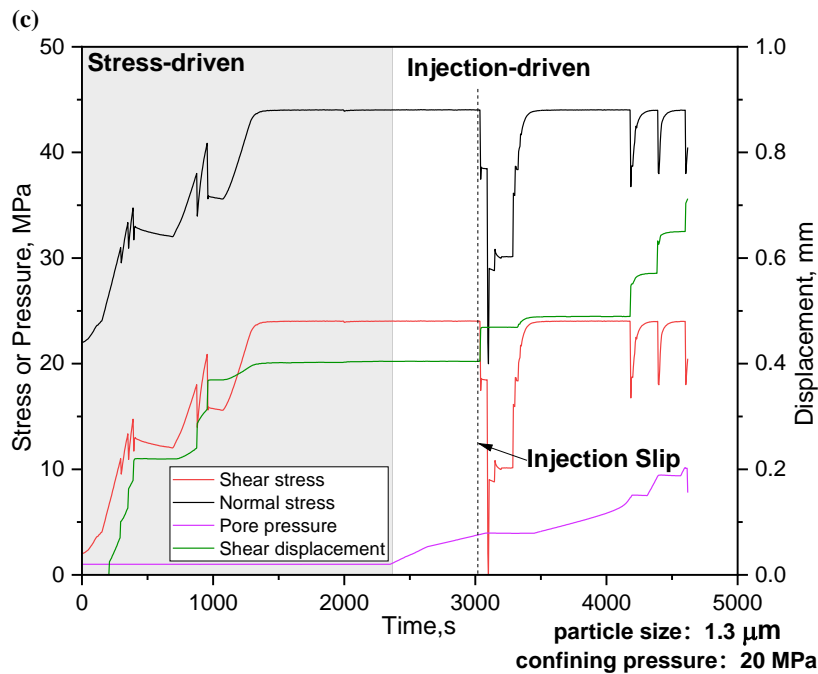
225   MPa.

226   Following the stress-driven reactivations, the samples were again reactivated by fluid pressures –

227   and again reactivated in contrasting styles according to fault roughness. For smooth rock samples,

228   a continuous stick-slip phenomenon occurred during the fluid injection.

229

(b)

230

(c)

231
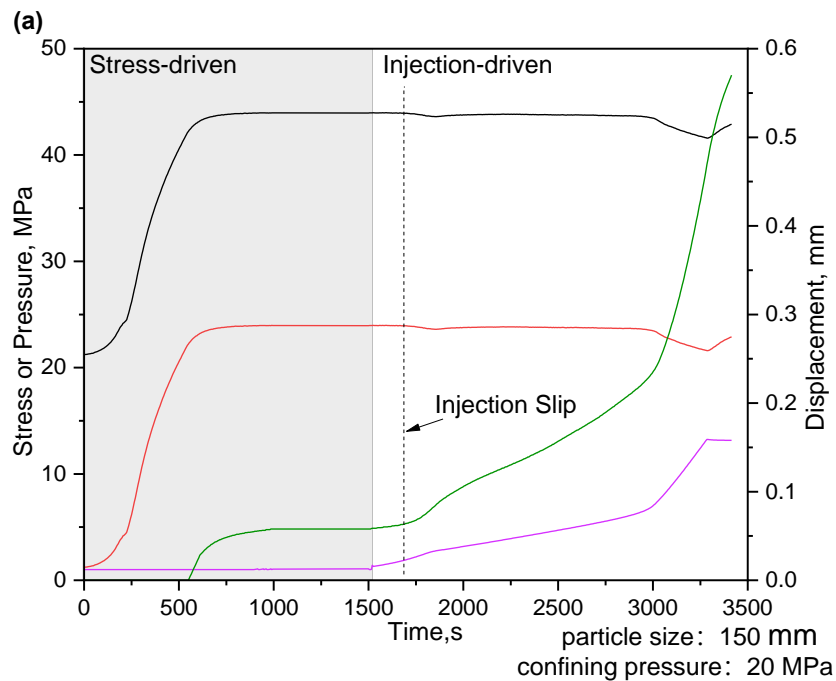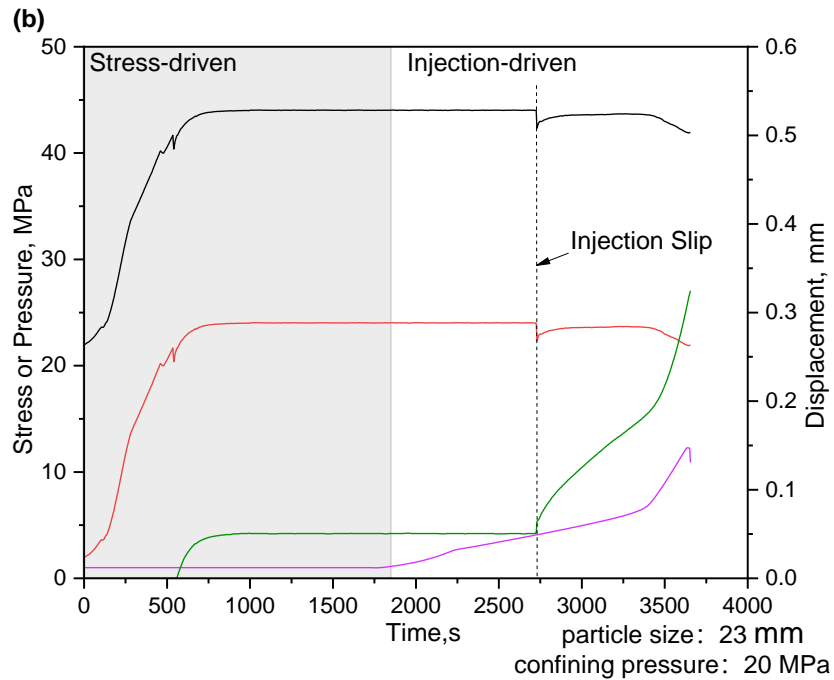
Figure 2. Stress, displacement, and pore pressure histories for the stress- and fluid-pressure-driven

reactivation experiments: (a) Rough sample 1-2, (b) Intermediate roughness sample 2-2, and (c)

smooth sample 3-2. The first half of the time history is under stress-driven conditions and the

second half under fluid-pressure-driven conditions.

236 The effective normal stress σ_{en} on the fault surface is equal to the difference between the normal

237 stress σ_n and pore pressure P_W as:

238
$$\sigma_{en} = \sigma_n - P_w \tag{8}$$

239 Figure 3 shows the Mohr-Coulmb failure envelopes for the faults during stress-driven and fluid-

240 pressure-driven reactivations. We construct the failure envelopes for the faults by fitting the shear

241 strengths obtained from the stress-driven frictional slip experiment, and derive the maximum static

242 friction coefficients for the faults polished by 150 μm, 23 μm, and 1.3 μm grit sandpapers as 0.53,

243 0.50, and 0.24, respectively. The shear stress on the faults gradually increased and then remained

244 constant after axial loading was stopped. Fluid was then injected into the fault at a constant

245 injection rate and the effective normal stress reduced. Although the fault was already critically

246 stressed, the fault does not reactivate until its stress state reaches a new envelope (blue dashed line).

247 The pore pressure measured from the injection boreholes is thus larger than that predicted by the

248 failure criterion. This is similar to the overpressure phenomenon found in other experiments and

249 field studies (Kakurina et al., 2019; Rutter & Hackston, 2017; Cappa et al., 2019) representing a

250 higher reactivation friction coefficient for fluid injection versus a change in total stress.

251
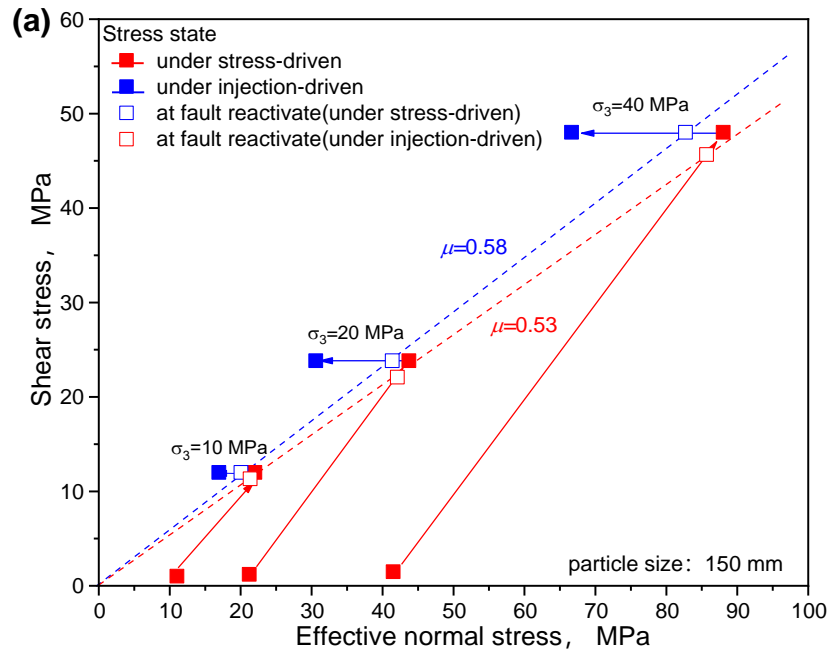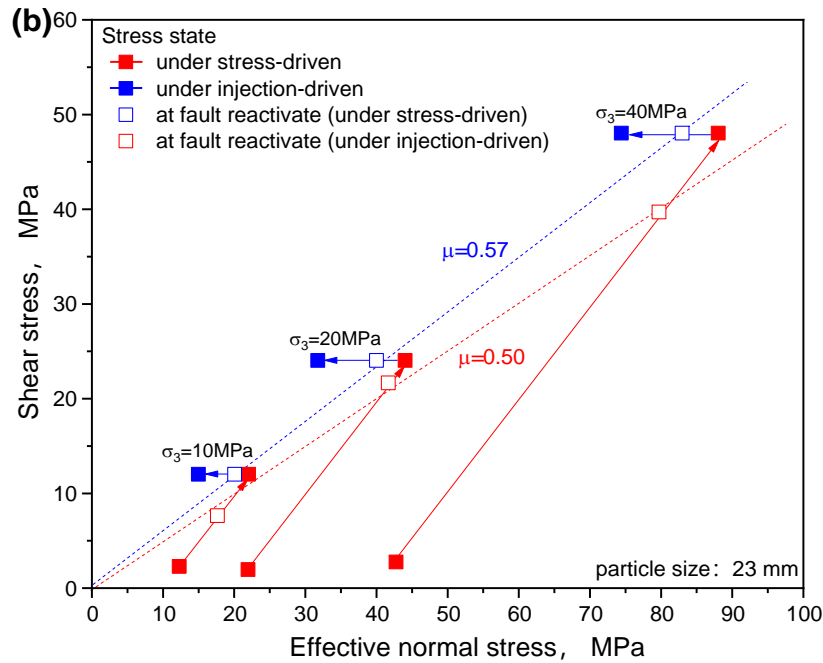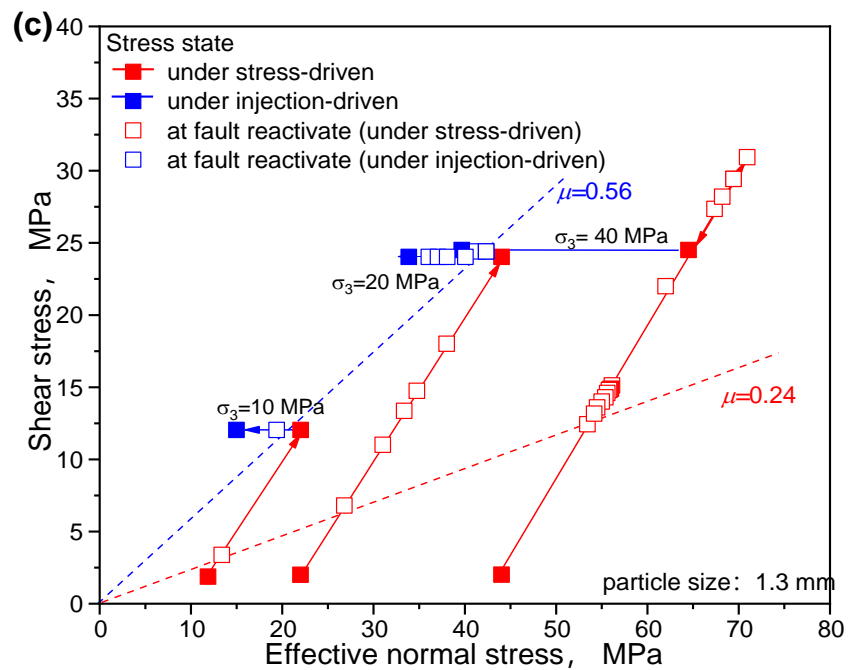
Figure 3. Mohr-Coulmb failure envelopes for laboratory faults reactivated by stress- and fluid-pressure-driven: (a) Samples polished to 150 μm roughness under confining pressures of 10 MPa, 20 MPa, and 40 MPa; (b) Samples polished to 23 μm roughness under confining pressures of 10 MPa, 20 MPa, and 40 MPa; (c) Samples polished to 1.3 μm roughness under confining pressures of 10 MPa, 20 MPa, and 40 MPa.

258   3.2 Fault damage characteristics

259   A three-dimensional (3-D) laser scanning system, with a 10-µm resolution laser beam, was used

260   to measure the topography of the fault surfaces. Typical profiles of the fault surface both before

261   and then after slip are shown in Figure 4. The main signature of the reactivation deformation is

262   striations as damage along the slip direction. After the test, the fault surface was observed by

263   microscope and no wear products were present on the fault surface. This is consistent with the

264   phenomena observed in previous studies (Ye and Ghassemi, 2018; Bijay and Ghazanfari, 2021;

265   Vogler et al., 2016). In this case, the smooth saw-cut fault does not develop a significant gouge

266   layer during the reactivation. The fault surface only produces a small amount of damage as concave

267   striations.

268   The volume of the concave striations on the fault surface caused by the damage was used to

269   characterize the damage on the fault surface during slip (Zhao et al., 2018b). This is equivalent to

270   the height and the area of the concave striations. The damage volume of each fault (shown in Table

271   2) is minute as compared to rough natural faults (Ji & Wu, 2020). This indicates that the surface

272   damage of the sawcut fault used in this work is much less than that of natural faults.

273   Fault slip characteristics are also affected by the uneven distribution of fault surface roughness

274   (Cappa et al., 2022). The roughness of the fault surface is uniformly distributed before the test.

275   However, it is possible to reorganize the distribution of roughness during slip due to the uneven

276   distribution of damage. We use the standard deviation of fault damage depth to characterize the

277   heterogeneity of fault damage (shown in Table 2). The standard deviation of each rock sample is

278   small, at 0.04~0.07 μm, indicating that the damage distribution on the fault surface is relatively

279   uniform.

280   For these reasons, the influence of fault gouge and the uneven distribution of fault surface

281   roughness caused by wear is neglected in the discussion that follows.

282
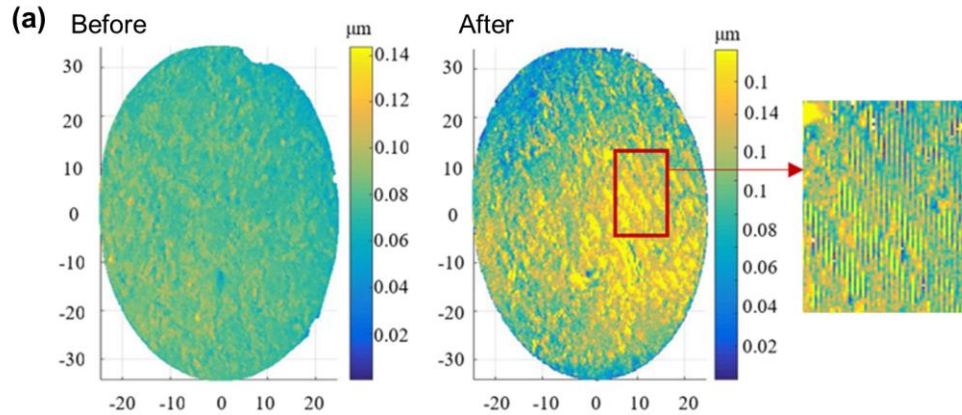
Figure 4. Damage on fault surfaces during reactivation: (a) Typical scanning results of a fracture
surface.

Table 2. The standard deviation of damage on fractured rock samples.

Sample number	Confining pressure （MPa）	Damage standard deviation （μm）			Volume of damage （mm^3）
		A	B	Average	
1-1	10	0.0482	0.0441	0.04615	2.711
1-2	20	0.0408	0.0474	0.0441	2.729
1-3	40	0.0497	0.0561	0.0529	2.769
2-1	10	0.0469	0.0429	0.0449	2.748
2-2	20	0.0417	0.0409	0.0413	2.762
2-3	40	0.0444	0.0616	0.053	2.788
3-1	10	0.0536	0.0511	0.05235	2.641
3-2	20	0.0495	0.0487	0.0491	2.665
3-3	40	0.049	0.0672	0.0581	2.695

3.3 Fault permeability characteristics

Fault slip reactivation may substantially affect the aperture of faults and hence permeability.
Permeability may change in sense depending on the mineral composition, stress conditions,
surface roughness, and shear displacement of the rock (Fang & Wu, 2022). Fault permeability also
influences the rate of pore pressure diffusion within the fault. In this study, the permeability of
faults has been measured from the initial state, after both stress-driven fault reactivation and then
after fluid-pressure-driven fault reactivation, respectively. These results are catalogued in the
supporting information S3. To obtain the evolution of permeability under fault reactivation, the
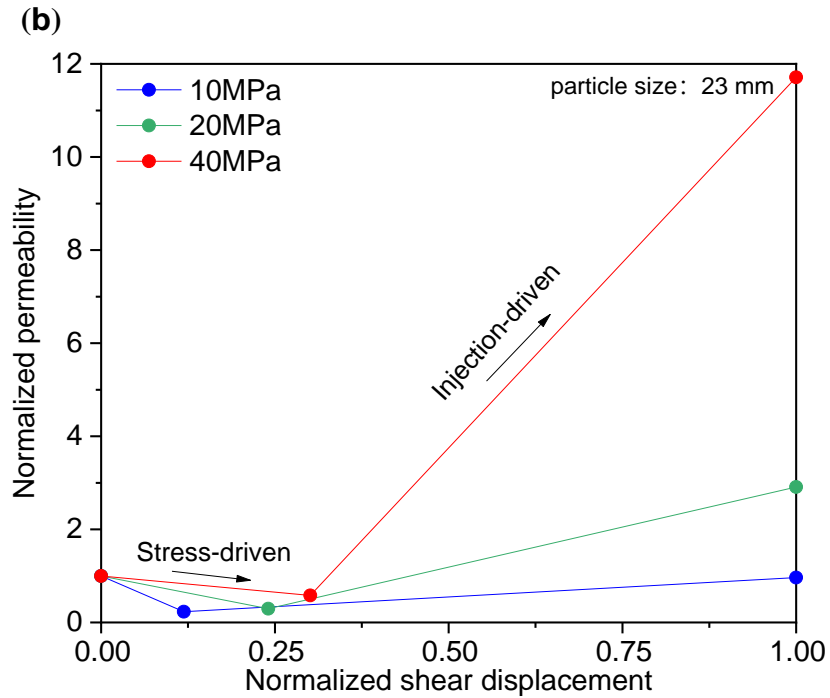fault permeability and shear displacements were normalized with respect to the initial permeability
and maximum shear displacement following reactivation.

298   Figure 5 shows the normalized permeability and the normalized shear displacement of the various

299   faults after stress-driven reactivation. The fault permeability decreases with an increase in shear

300   displacement as a result of fault compaction under stress-drive (Ishibashi et al., 2018; Jia et al.,

301   2020; Fang & Wu, 2022). For a natural rough fault, the evolution of asperity geometry and

302   distribution modifies the fracture aperture and the flow velocity and subsequently enhancement

303   the fault permeability (Ye and Ghassemi, 2018). However, the smooth fault surfaces in this study

304   cannot drive significant fracture dilation. The fault damage characteristics noted in Section 3.2,

305   representing shallow striations of damage on the fault surface, do not promote significant shear

306   dilatancy.

307   The fault permeability increased under fluid-pressure-driven. This is opposite to the trend in

308   permeability change under stress-driven condition. In this condition, the major contributor to

309   permeability enhancement is the normal dilation resulting from the increase of pore pressure in

310   fault. The permeability enhancement during fracture shearing is highly dependent on fault

311   roughness and stress state (Ye and Ghassemi, 2018). For a low-roughness fault at high stress, a

312   rapid slip with an associated large stress drop is induced under injection-driven reactivation,

313   creating a much larger increase in fracture permeability. This results in a significant increase in the

314   permeability of smooth faults, up to 36 times higher than the initial permeability (Figure 5c).

315

(b)

316

(c)
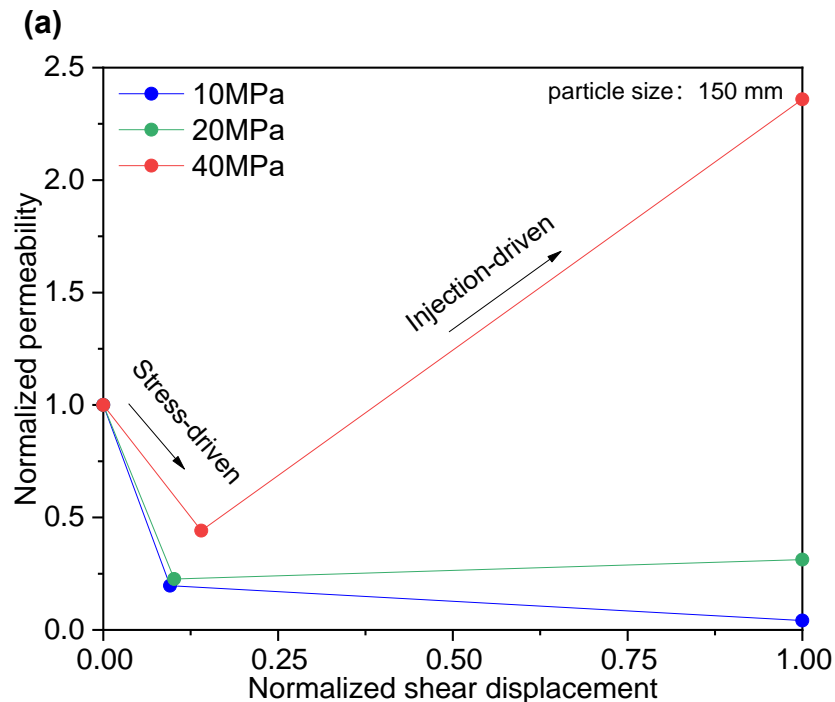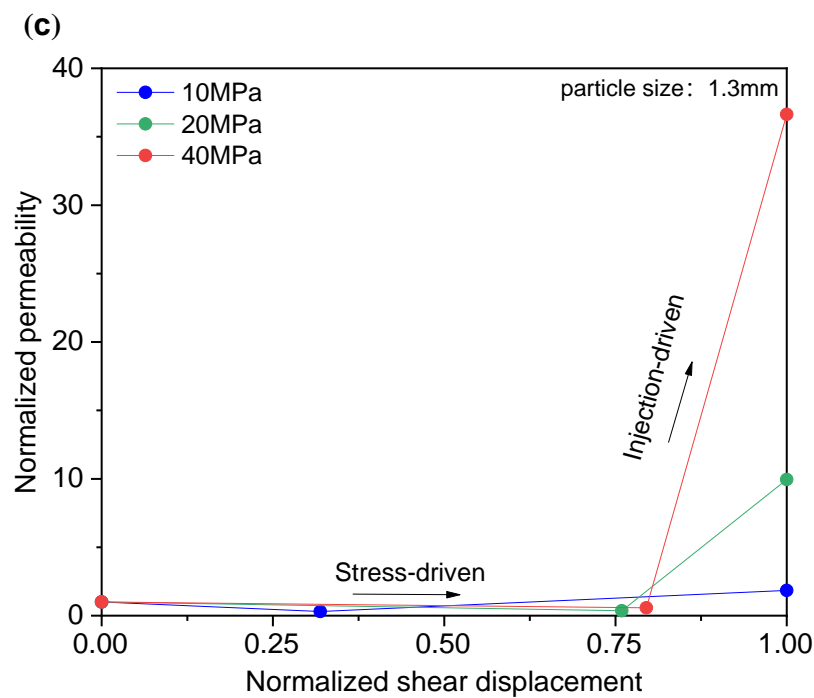
317

318   **Figure 5.** Normalized fracture permeability as a function of normalized shear displacement: (a)

319   Samples polished to 150 μm roughness under confining pressures of 10 MPa, 20 MPa, and 40 MPa;

320   (b) Samples polished to 23 μm roughness under confining pressures of 10 MPa, 20 MPa, and 40

321   MPa; (c) Samples polished to 1.3 μm roughness under confining pressures of 10 MPa, 20 MPa, and

322   40 MPa.

323 **4 Discussion**

324 4.1 Mechanism of fault activation under stress-drive conditions

325 The mechanism of fault slip under stress-drive conditions may be explored by investigating the

326 evolution of mechanical properties (shear and normal stress, shear displacement, friction

327 coefficient and shear velocity). It is suggested that data sampled at less than 10 Hz may

328 underestimate the values of the dynamic slip events (McLaskey & Yamashita, 2017; Passelègue

329 et al., 2019). Therefore, we will not discuss the rate of fault slip. In Figure 6, The friction

330 coefficient is obtained by the ratio of shear stress to normal stress. Three stages of fault reactivation

331 can be defined under stress-drive conditions according to the evolution of shear displacement:

332 **(1) Stability stage:** The shear displacement is kept at zero during the stress loading. The shear

333 stress remains below that of static friction and the fault remains stable.

334 **(2) Initial slip stage:** Shear stress exceeds the peak static friction and shear displacement begins

335 to increase. The shear displacement increases linearly with the shear stress after an acceleration.

336 At this time, the fault enters a steady-state initial condition after the initial run-in period.

337 **(3) Continuous slip stage:** As the axial stress continues to increase, high roughness faults (Figure

338 6a, using a representative example of sample 1-3 with all other results catalogued in the supporting

339 information S1) remain in stable-slip and the friction coefficient increases with slip. For a smooth

340 fault, the fault reactivates in stick-slip with a stress drop and shear displacement. The friction

341 coefficient changes from the maximum static friction coefficient to the dynamic friction coefficient

342 during this period. With an increase in the normal stress and shear stress, the friction coefficient

343 gradually increases until the loading stops or the next stick-slip occurs.

344

345
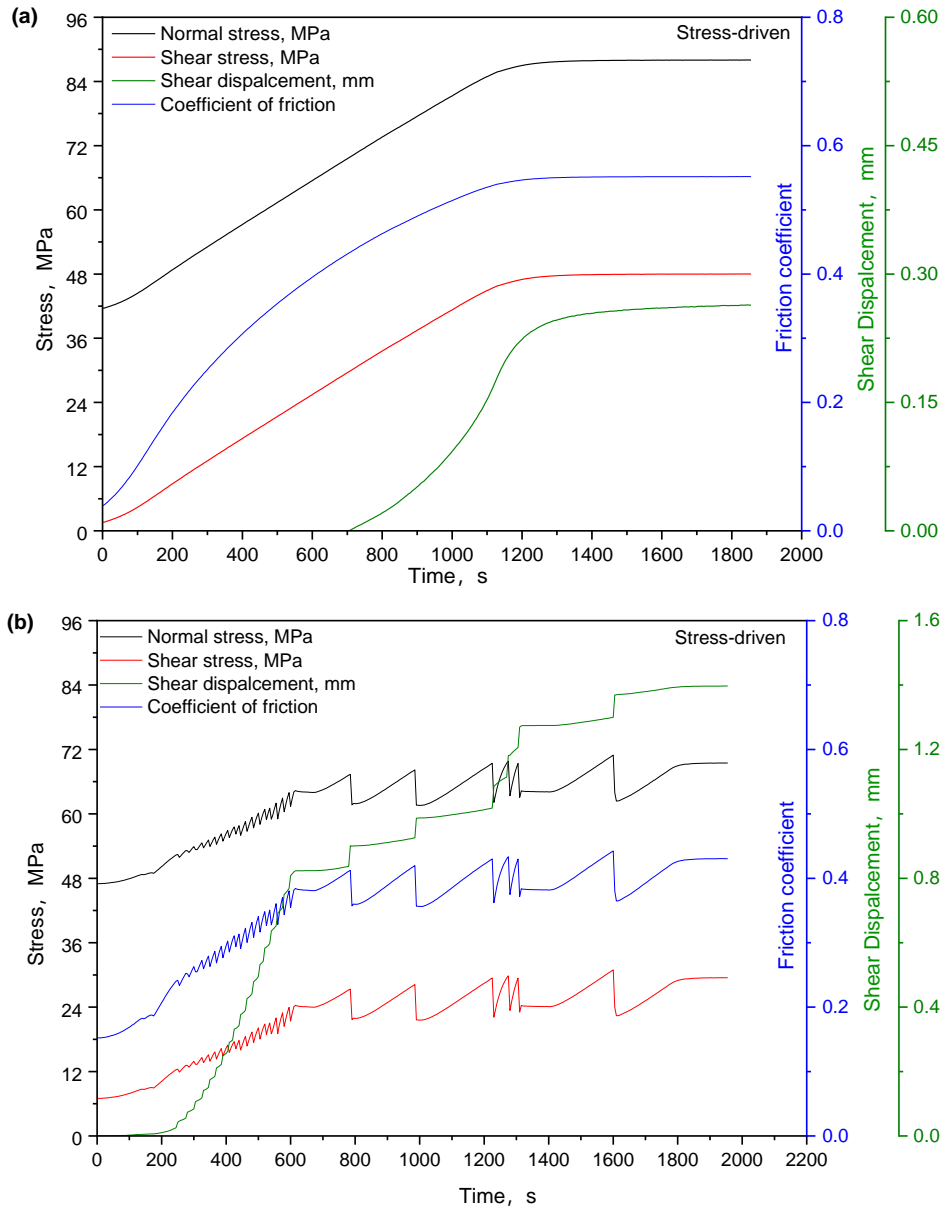
Figure 6. Change in mechanical properties during stress-driven frictional slip: (a) Stable-slip; (b) Stick-slip.

According to the three stages of fault slip, the change in friction coefficient is related to the fault stress state, slip distance, and slip characteristics (stable-slip or stick-slip) during continuous stress loading. At present, the four most widely used models to describe fault slip are rate weakening (Tsutsumi and Shimamoto, 1997), rate- and state-dependent models with either an aging law (Dieterich, 1978) or slip law (Ruina, 1983), and slip weakening friction (Ida, 1972). Among them, the first three require rate data during slip. These data are difficult to recover for practical engineering applications. According to the friction law related to slip weakening, the change in

355 friction coefficient with slip shows a linear or nonlinear relationship. The friction relationship for

356 slip weakening under linear conditions can be described as (Ida, 1972):

357
$$\tau = \begin{cases} \left[\mu_s - \left(\mu_s - \mu_f \right) \dfrac{u}{d_0} \right] \sigma_n & ,u < d_0 \\ \mu_f \sigma_n & ,u \geq d_0 \end{cases} \tag{9}$$

358 where μ_f and μ_s are the maximum dynamic friction coefficient and static friction coefficient,

359 respectively; u is the relative slip displacement between upper and lower fault surfaces; σ_n is the

360 normal stress on the fault surface; d_0 is the characteristic slip distance, representing the slip distance

361 required for the static friction coefficient to decrease to the dynamic friction coefficient.

362 Therefore, the analysis of friction slip mechanism of faults under stress-driven condition can be

363 described as follows: As shown in Figure 7a, the transition from the initially stable stage to slip

364 can be explained by the Mohr-Coulmb failure criterion. Fault slip occurs when the shear stress on

365 the fault exceeds its maximum static frictional resistance. Faults with a high roughness faults

366 mainly return stable slip (Figure 7b). In this circumstance, the maximum static friction coefficient

367 of the fault μ_s and dynamic friction coefficient μ_f are equal. Thus, Eq. (9) becomes

368
$$\tau = \mu_f \sigma_n = \mu_s \sigma_n \tag{10}$$

369 Considering the influence of fault angle, substituting Eqs. (4) and (5) into Eq. (10) yields,

370
$$\mu_s = \mu_f = \frac{\tau}{\sigma_n} = \frac{\left(\sigma_1 - \sigma_3 \right) \cos \beta \sin \beta}{\sigma_1 \sin^2 \beta - \sigma_3 \cos^2 \beta} \tag{11}$$

371 It is apparent from Eq. (11) that in the fault strengthening stage, the fault friction coefficient is

372 mainly related to the stress level and the angle of fault surface. As shown in Figure 7c, the fault

373 slips by shear offset d_1 at the onset of the first stick-slip event. The stress drop on the fault surface

374 changes according to the difference in the static friction coefficient μ_{s1} to the dynamic friction

375 coefficient μ_{f1}. The frictional slip characteristics of the fault surface still conform to Eq. (9). Then,

376 as the stress continues to increase, the fault strengthens and the friction coefficient gradually

377 increases. At this time, the fault slips stably, which conforms to Eqs. (10) and (11). During fault

378 slip, the maximum static friction coefficient changes from μ_{S1} to μ_{s2}. When the fault friction

379 coefficient grows to a new maximum static friction coefficient μ_{s1} during the fault strengthening,

380 the fault becomes stick-slips again. This cycle is repeated until the loading stops.
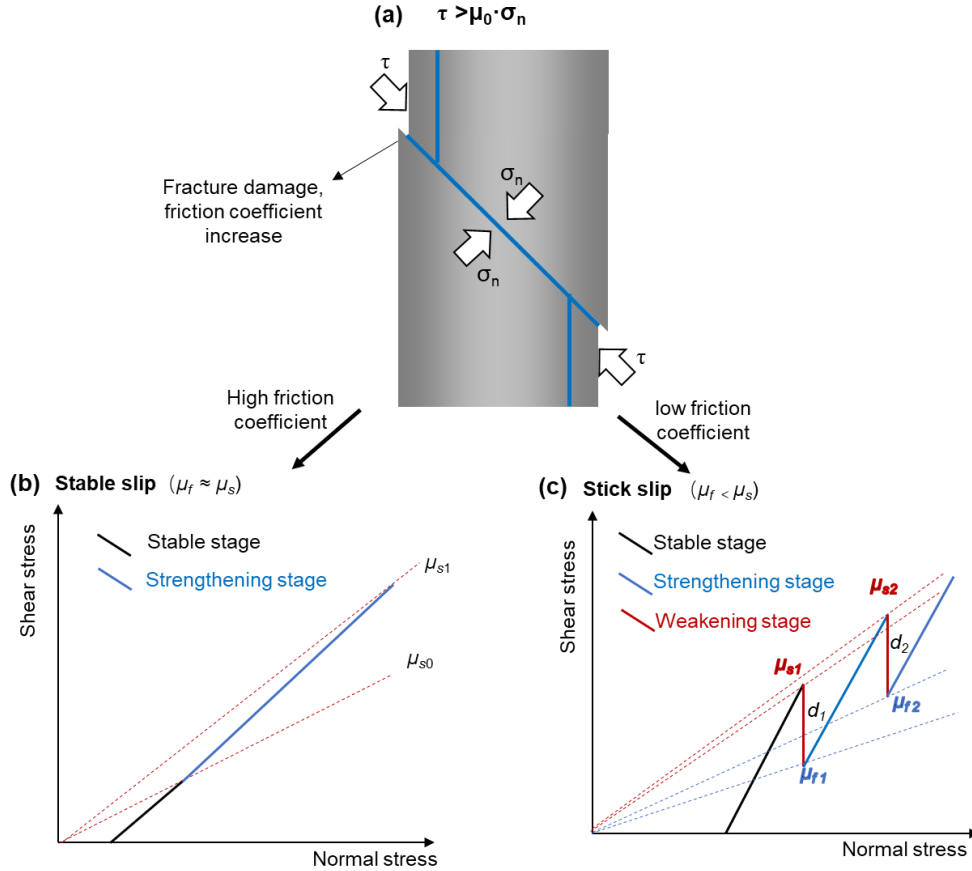
Figure 7. Mechanisms of fault reactivation under stress-driven: (a) Schematic of fault instability; (b) Stable slip under stress-driven conditions; (c) Stick-slip under stress-driven conditions.

Therefore, the slip-weakening law under linear conditions may be modified and the slip-weakening law during fault strengthening and continuous stick-slip proposed as:

$$
\tau = \begin{cases} \left[\mu_{si} - \left(\mu_{si} - \mu_{fi} \right) \dfrac{u}{d_i} \right] \sigma_n & D_i < u < D_i + d_i \\[2em] \dfrac{\left(\sigma_1 - \sigma_3 \right) \cos \beta \sin \beta}{\sigma_1 \sin^2 \beta - \sigma_3 \cos^2 \beta} \sigma_n & d_i < u < D_{i+1} \end{cases}
$$

(12)

where i is the stick-slip event sequence number, d_i is the slip distance required for friction to drop from static to dynamic for the ith stick-slip, $\mu_{si,}$ and μ_{fi} are the static friction coefficient and the dynamic friction coefficient for the ith stick-slip, and D_i is the length of fault slip before the ith stick-slip. When the fault is in its stable slip stage, the characteristic slip distance of the fault $d_i = 0$, and Eq. (12) returns Eq. (11). Therefore, Eq. (12) can characterize both stable slip and stick-slip events.

393   In addition, when using Eq. (12) to calculate frictional slip, it is necessary to obtain the

394   characteristic slip length d_i. In stick slip, the slip distance of the fracture is often related to the

395   difference in the stress on the fracture surface from before until after slip (Mohammadioun, 2001).

396   The stress drop is calculated as:

$$\Delta\sigma = \sigma_0 - \sigma_1 \tag{13}$$

397

398   If the stress drop distribution of historical earthquakes is known, then the dynamic process of

399   earthquake rupture may be illuminated. The characteristic slip length d_i increases with the stress

400   drop. Because of the non-uniform distribution of stress and strength near the fault, the relationship

401   between slip distance and stress drop is generally complex. Two methods are primarily used to

402   evaluate stress drop. The first is to apply a scaling relationship based on comparing the earthquake

403   magnitude with its radiated energy or the estimated fault rupture area (Andrews, 2013). The second

404   is to estimate the stress drop by finding the relevant parameters in the model through a source

405   spectrum analysis based on an assumed source model. Where the source spectrum analysis is used,

406   a disc fault model is generally assumed for small and medium-sized earthquakes. Here, a disk of

407   radius R, is subject to a stress drop $\Delta\sigma$ as

$$\Delta\sigma = \frac{7}{16} \cdot \frac{M_0}{R^3} \tag{14}$$

408

409   where M_0 is the seismic moment. This moment may be evaluated from the shear modulus G of

410   the fractured rock mass (Aki, 1966) as,

$$M_0 = GSd \tag{15}$$

411

412   where, S is the area of the fault, m^2. G can be considered as the combined rigidity of the test system

413   and the fracture and can be determined based on the least squares method to achieve the minimum

414   value of the sum of squared residuals (Ji et al. 2019):

$$G = \frac{M_0 \sum_{i=1}^{n} d_i}{S \sum_{i=1}^{n} (d_i^2)} \tag{16}$$

415

416   Figure 8 shows the relationship between slip distance and stress drop during the stick-slip cycle.

417   The trends of stress drop and slip displacement remain the same under both stress- and injection-

418   drive. The combined rigidity is recovered from the least squares method and results in a best-fit

419   value of 0.55 GPa (R^2=0.90). The fitting results agree well with the stress drop and slip

420   displacement measured directly in the tests, indicating that the derived rigidity is reasonable. By

421   monitoring the magnitude of the stress drop on the fault surface, the characteristic slip value d_i can

422   be obtained, and the entire fault slip process followed.
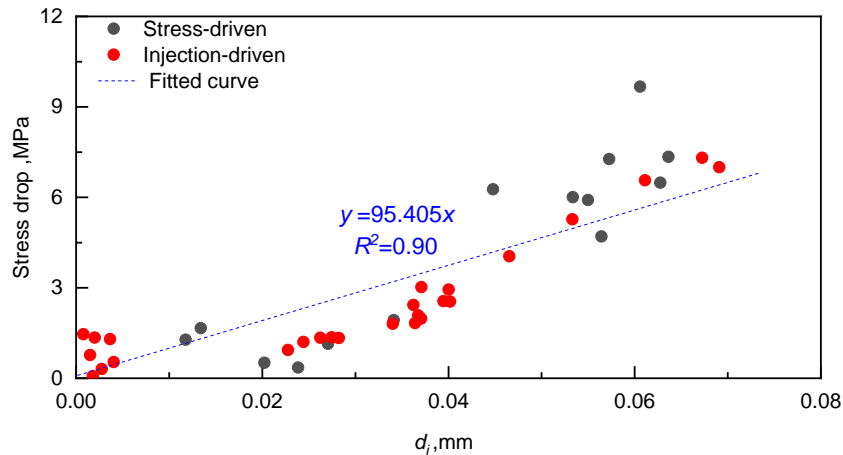
423

424   **Figure 8.** Stress drop with slip distance. Black points are the experimental data under stress-drive;

425   Red points are the experimental data under injection-drive. The blue dotted line is obtained by

426   jointly fitting the experimental data under stress-drive and injection-drive.

427   4.2 Mechanism of fault reactivation under fluid-pressure-driven condition

428   Figure 9 shows typical slip distance versus friction coefficient results for stable slip and stick–slip

429   processes. Frictional slip under fluid-pressure-drive can also be divided into three stages: a stable

430   stage, an initial slip stage then a continuous slip stage, similar to the slip characteristics under

431   stress-drive. In the stable stage, despite the increase in pore pressure, the fault does not slip. In the

432   initial slip stage, when the pore pressure increases to a threshold, the fault shows stick–slip. In the

433   continuous slip stage, and with the continued fluid injection, the fracture stick-slips several times

434   and this remains the predominant mode of slip.
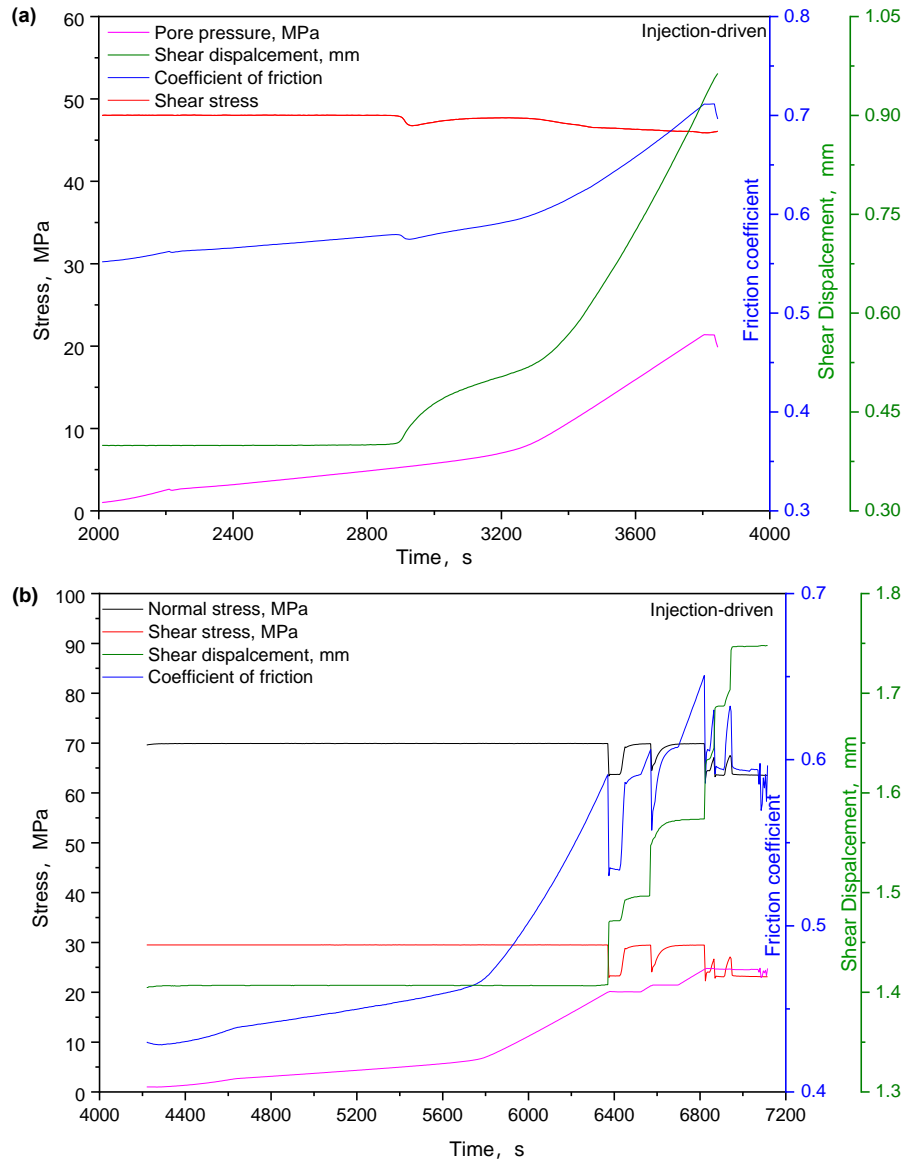
Figure 9. Evolution of mechanical properties under injection-drive: (a) Smooth fault; (b) Rough fault.

The faults in the pressure-drive tests have already slipped in the preceding stress-drive portion of the test. The faults did not slip during the stable stage of fluid injection, indicating that the pore pressure in the fault injection borehole is higher than the pore pressure predicted by the Mohr-Coulmb failure criterion. An overpressure ratio (Ji et al., 2021) may be defined as the ratio of fluid pressure increase measured at the injection borehole at the beginning of fault instability to the pore pressure predicted by the failure criterion. It can be shown that the fluid overpressure is related to initial normal stress, shear stress and injection rate (Ji & Wu, 2020; Ji et al., 2021; Passelègue et al., 2018). However, for a critically stressed fault, the Mohr-Coulmb failure criterion predicts a

447   fluid pressure of 0, and the overpressure ratio of the fault cannot be calculated. Moreover, the fault

448   overpressure ratio is strongly influenced by the fault initial stress state. Even for the same fault,

449   different overpressure ratios might be obtained under different stress states. Therefore, we only

450   study the effect of the overpressure on the reactivation of faults. Considering the effect of

451   overpressure(P_{over}), the pore pressure effective stress criterion can be modified as:

452
$$
\begin{cases}
\sigma_{en} = \sigma_n & , P_w \leq P_{over} \\
\sigma_{en} = \sigma_n - \overline{P_w} - P_{over} & , P_w > P_{over}
\end{cases}
\tag{17}
$$

453   where $\overline{P_w}$ is the equivalent pore pressure in the fault.

454   The fluid overpressure is constant when the fluid distribution is uniform on faults and increases

455   with a more heterogeneous fault pressure distribution as demonstrated by Passelègue et al. (2018).

456   The fluid pressure distribution on a fault depends on the balance between fluid injection and

457   diffusion rates (Ji et al., 2022). A faster rate of fluid injection promotes high gradients around the

458   injection point (Ji & Wu, 2020; Ji et al., 2021; Passelègue et al., 2018). The rate of fluid injection

459   can be artificially controlled. However, the heterogeneous fault pressure distribution is related to

460   heterogeneity of the fault itself. As shown in Figure 10, the slip zone has a high pore pressure and

461   is reactivated during the injection. The remainder of the fault remains locked. In the initial stage

462   of fluid injection, although the pore pressure in the injection boreholes is gradually increased, the

463   locked area retains the fault stable.

464
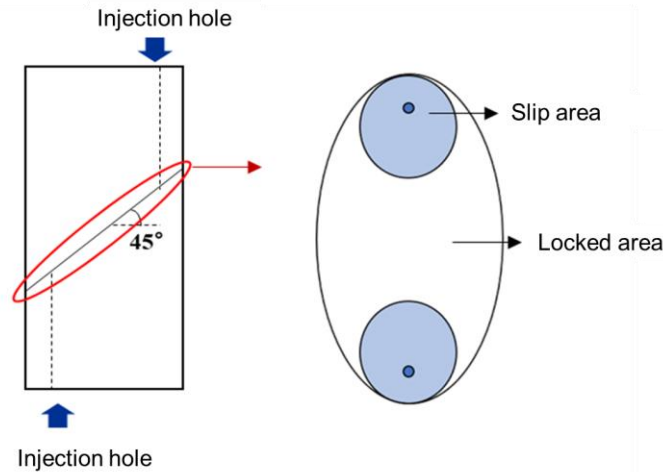
465   **Figure 10.** Locked and slipping zones on faults. The blue area is the slip area embedded within

466   the (white) locked area.

467   The rate of pressure diffusion within the fault as expressed by the diffusion coefficient A, defined

468   as:

469 $$A = k / \mu\alpha\Phi \qquad (18)$$

470   where μ is fluid viscosity, α is fluid compressibility, Φ is the fault porosity and k is the fault

471   permeability. As the fluid compressibility and dynamic viscosity, together with the fault porosity

472   of each rock sample have the same value, the fault diffusion coefficient is a function of

473   permeability. Therefore, the rate of pressure diffusion could also be characterized by permeability,

474   which is an extremely important property for EGS projects. The relationship between overpressure

475   and fault permeability, measured before fluid-pressure-driven reactivation, is shown in Figure 11

476   as a negative exponential relationship between the overpressure P_{over} and fault permeability k.
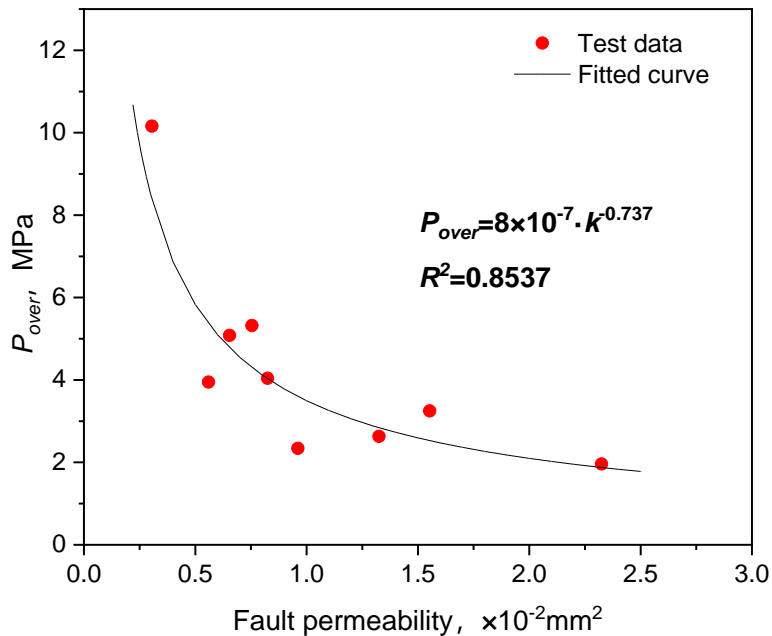
477

478   **Figure 11.** Fluid overpressure and fault permeability recovered from first slip on faults that
479   exhibited significant stick-slip.

480

481   The mechanism of fault slip under pressure-drive is shown in Figure 12. During fluid injection,

482   the shear stress produced by faults did not change in the initial stage due to the presence of

483   overpressure, but decreased with the decreasing effective normal stress after the pore pressure

484   exceeded the overpressure. The fault exhibited stick–slip response due to the combined mechanical

485   and fluid loads during the increase of pore pressure, and a stress drop occurred. Subsequently, the

486   stress path exhibits nonlinearity due to slip-strengthening and permeability evolution. During the

487   strengthening process, the fluid pressure again increases, leading to continuous stick-slip response

488   in the smooth faults. The evolution of friction coefficient and permeability are the main factors

489   influencing fluid-injection-induced earthquakes and are both related to fault roughness.
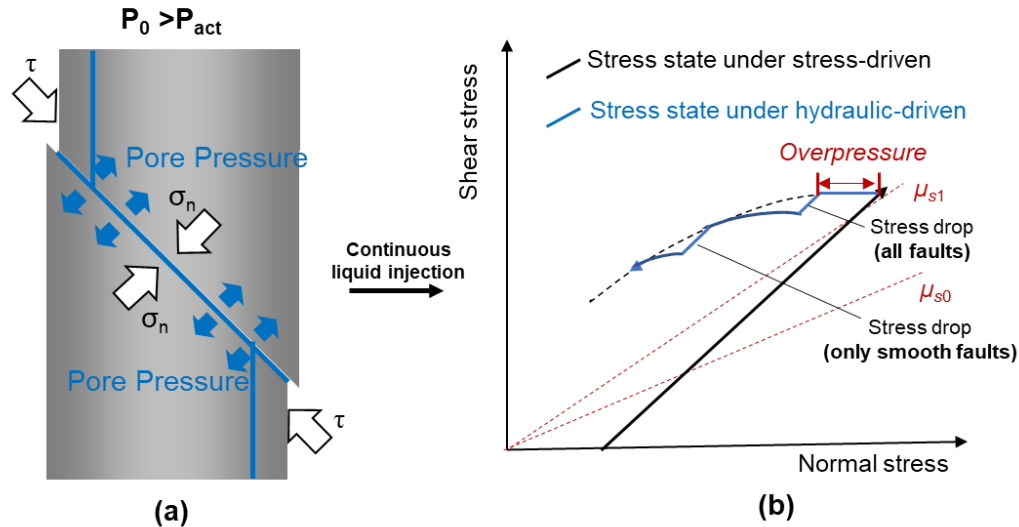
490
491   **Figure 12.** Mechanism of faults reactivation under fluid-pressure-drive -driven: (a) Schematic of

492   fault instability; (b)Stress path of faults slip under fluid-pressure-driven.

493   4.3 Implications for injection-induced seismicity

494   During fluid injection, the fault is subjected to the combined effects of both stress and fluid

495   pressure. It is important to fully understand the mechanisms of stress- and fluid-pressure-driven

496   fault reactivation for the better assessment and control of induced earthquakes. We obtain the

497   frictional slip characteristics of faults under stress- and fluid-pressure-driven conditions through a

498   series of triaxial shear tests. The fault frictional slip characteristics are shown to be closely related

499   to the roughness and permeability of the fault.

500   By comparing the stress- and hydraulic-driven fault slip characteristics, it is observed that under

501   stress-driven conditions, stick–slips occurred only on the smoother faults. However, natural faults

502   with a rougher surface showed stick–slip only at very high stress levels. For fluid injection, even

503   the rough faults showed stick–slip response. This indicates that the risk of inducing earthquakes is

504   extremely high once the fault slips as a result of fluid injection. For example, the Duvernay

505   hydraulic fracturing project in Western Canada (Bao et al., 2016; Eyre et al., 2019a; Eyre et al.,

506   2019b) and shale gas extraction in the central and eastern United States (Ellsworth et al., 2013;

507   Keranen et al., 2014;) and EGS projects in Switzerland (Elsworth et al., 2016; Majer et al., 2007),

508   and South Korea (Kim et al., 2018; Grigoli et al., 2018) have all generated induced earthquakes.

509   At present, our determination of fault state is mainly based on the Mohr-Coulmb failure criterion

510   and effective stress criterion. Fault slip is mainly influenced by the applied stresses and fault

511   friction coefficient. For a fault in a critical state, the effective stress will decrease after liquid

512   injection and the fault should slip immediately. However, the results of fluid injection induced

513   seismicity in the central United States indicates that seismicity occurs potentially long after the

514   injection (Keranen et al., 2013). This is potentially due to the uneven distribution of pore pressure

515   within the fault, resulting in the fluid pressure required for fault activation often being higher than

516   the value predicted by applying the Mohr-Coulmb failure criterion. The difference is the

517   overpressure, making it difficult to determine the timing of injection-induced seismicity. During

518   the injection, the pore pressure distribution in the fault is affected by various factors such as fault

519   roughness, stress state, mineral composition, and fluid injection conditions (Fang & Wu, 2022),

520   resulting in a complex behavior. This experimental study shows that the overpressure required for

521   fault reactivation is related to its permeability. Fluid injection into EGS reservoirs will elevate

522   permeability from micro- to milli-Darcy levels. This may reduce the pore pressure required for

523   fault reactivation and increase the risk of induced earthquakes. Therefore, during EGS fluid

524   injection, chemical and physical means can be used to stimulate the fault to increase its roughness,

525   thereby reducing the risk of fluid injection induced earthquakes.

526   Finally, it is necessary to point out that the vast majority of previous studies on fluid injection

527   induced earthquakes, whether from laboratory or field perspectives, focused more on the instability

528   behavior of optimal faults under regional tectonic stress state. According to the Mohr-Coulmb

529   criterion, the angle between the optimally orientated fault and the maximum principal stress is

530    $45°–0.5\tan^{-1}\mu$. Byerlee (1978) indicated that for most rocks, the friction coefficient of the fault is

531   ~0.6, corresponding to an optimal azimuth angle of ~30°. The 45° angle in this study is not the

532   optimal fault orientation, regardless of the friction coefficients obtained from sawcut faults with

533   various roughness. Due to the minimum shear stress required for the initiation of fault slip along

534   the favorable direction, previous study results only provided the lower limit of fluid overpressure

535   during fault slip (Ji et al., 2022). Hence, the results of our overpressure experiment may be more

536   universally representative. It is necessary to pay more attention to the study of fluid injection

537   induced earthquakes in unfavorably orientated faults in the future.

5 Conclusions

To obtain the slip characteristics of faults under both stress- and fluid-pressure-induced reactivation, we completed laboratory reactivation experiments on three groups of saw-cut faults with different roughnesses. The results show that under the stress-drive conditions, a rougher slips stably, suggesting slip strengthening and smoother faults reactivate in stick-slip mode - first exhibiting weak slip and then slip strengthening. Under pressure-driven condition, the uneven distribution of pore pressure results in fault slip only after the pore pressure within the fault increased to a significant overpressure. The magnitude of this overpressure is related to permeability with overpressure increasing with a decrease in permeability. The results potentially improve our ability to develop successful EGS projects and mitigate the risk of anthropogenic earthquakes in EGS.

Data Availability Statement

This manuscript is accompanied by Supporting Information. The experimental data presented in this study are available at https://doi.org/10.5061/dryad.vt4b8gtws.

References

Aki, K. (1966). Generation and propagation of G waves from the Niigata earthquake of June 16, 1964. 2. Estimation of earthquake movement, released energy, and stress-strained drop from G wave spectrum. *Geology*, *44*(1),73-88,doi: 10.4236/ojer.2016.52007.

Andrews, D.J. (2013). *Objective Determination of Source Parameters and Similarity of Earthquakes of Different Size*. American Geophysical Union (AGU).

Bao, X., & Eaton, D. W. (2016). Fault activation by hydraulic fracturing in western Canada. *Science*, *354*(6318), 1406–1409, doi:10.1126/science.aag2583.

Bijay, K. C. , & Ghazanfari, E. (2021). Geothermal reservoir stimulation through hydro-shearing: an experimental study under conditions close to enhanced geothermal systems. *Geothermics*, *96*(5-6):102200, doi: 10.1016/j.geothermics.2021.102200.

568   Brace, W. F., Walsh J. B., & Frangos W. T.(1968). Permeability of granite under high pressure. *Journal of*
569   *Geophysical Research*, *73*(6), 2225-2236, doi: 10.1029/JB073i006p02225.

570   Byerlee, J. D. (1967). Frictional characteristics of granite under high confining pressure. *Journal of Geophysical*
571   *Research*, *72*(14), doi: 10.1029/JZ072i014p03639.

572   Cappa, F., Scuderi, M.M., Collettini, C., Guglielmi, Y., & Avouac, J.P. (2019). Stabilization of fault slip by fluid
573   injection in the laboratory and in situ. *Science Advances*, *5*(3), eaau4065, doi: 10.1126/sciadv. aau4065.

574   Cappa F., Guglielmi Y., Nussbaum C., De Barros L., & Birkholzer J. (2022). Fluid migration in low-permeability
575   faults driven by decoupling of fault slip and opening. *Nature Geoscience*, *15*, 747–751, doi:10.1038/S41561-
576   022-00993-4.

577   Chen, Y., Zhang, C., Zhao, Z., & Zhao, X. (2020). Shear Behavior of Artificial and Natural Granite Fractures
578   After Heating and Water-Cooling Treatment. *Rock Mechanics and Rock Engineering*, *53*(4–5), 5429–5449,
579   doi: 10.1007/s00603-020-02221-0.

580   Collettini, C. (2014). A novel and versatile apparatus for brittle rock deformation. *International Journal of Rock*
581   *Mechanics and Mining Sciences*, *66*,114-123, doi: 10.1016/j.ijrmms.2013.12.005.

582   Cornelio, C., Spagnuolo, E., Di Toro, G., Nielsen, S., & Violay, M. (2019). Mechanical behaviour of fluid-
583   lubricated faults. *Nature Communications*, *10*(1), 1274. doi: 10.1038/s41467-019-09293-9.

584   Dieterich, J. H. (1978). Time-Dependent Friction and the Mechanics of Stick-Slip. *pure and applied geophysics*,
585   *116*(4), 790-806, doi:10.1007/BF00876539.

586   Dieterich, J.H. (1979). Modeling of rock friction: 1. Experimental results and constitutive equations. *Journal of*
587   *Geophysical Research*. *84*(B5), 2161, doi: 10.1029/JB084IB05P02161.

588   Ellsworth, W.L. (2013). Injection-Induced earthquakes. *Science*, *341*(6142):1225942, doi:
589   10.1126/science.1225942.

590   Elsworth, D., Spiers J. C. & Niemeijer A. R. (2016). Understanding induced seismicity. Science, *6318*(354),
591   1380-1381, doi:10.1126/science.aal2584.

592   Eyre, T. S., Eaton, D. W., Megan, Z., David, D., & Danylo, K. (2019a). Microseismicity reveals fault activation
593   before mw 4.1 hydraulic-fracturing induced earthquake. *Geophysical Journal International*, *218*(1):534–46,
594   doi: 10.1093/gji/ggz168.

595   Eyre, T. S., Eaton, D. W., Garagash, D. I., Zecevic, M., & Lawton, D. C. (2019b). The role of aseismic slip in
596   hydraulic fracturing-induced seismicity. *Science Advances*, *5*(8), eaav7172, doi: 10.1126/sciadv.aav7172.

597   Fang, Z., & Wu, W. (2022). Laboratory friction-permeability response of rock fractures: a review and new
598   insights. *Geomechanics and Geophysics for Geo-Energy and Geo-Resources*. *8*(1), 15 ,doi:10.1007/s40948-
599   021-00316-8.

600   Galis, M., Ampuero, J.P., Mai, P.M., & Cappa, F. (2017). Induced seismicity provides insight into why
601   earthquake ruptures stop. *Science Advances*, *3*(12), 7528, doi:10.1126/sciadv.aap7528.

602 Grigoli, F., Cesca, S., Rinaldi, A. P., Manconi, A., López-Comino, J. A., & Clinton, J. F., et al. (2018). The
603   November 2017 Mw 5.5 Pohang earthquake: a possible case of induced seismicity in South Lorea. *Science*,
604   *360*(6392), 1003-1006, doi: 10.1126/science.aat2010.

605 Hao, M. Shen, Z., Wang, Q., & Cui, D. (2012). Postseismic deformation mechanisms of the 1990 Mw 6.4
606   Gonghe, China earthquake constrained using leveling measurements. *Tectonophysics*, 532–535, 205–214,
607   doi:10.1016/j.tecto.2012.02.005.

608 Ida, Y. (1972). Cohesive force across the tip of a longitudinal-shear crack and Griffith's specific surface energy.
609   *Journal of Geophysical Research*, *77*(20), 3796–3805, doi:10.1029/JB077i020p03796.

610 Ishibashi, T., Elsworth, D., Fang, Y., Riviere, J., Madara, B., Asanuma, H., Watanabe, N., & Marone, C. (2018).
611   Friction-Stability-Permeability Evolution of a Fracture in Granite. *Water Resources Research*, *54*(12), 9901–
612   9918, doi.:10.1029/2018WR022598.

613 Jaeger, J. C., Cook, N. G. W., & Zimmerman, R. (2009). *Fundamentals of rock mechanics*. John Wiley & Sons.

614 Ji, Y. , Hofmann, H. , Duan, K. , & Zang, A. (2022). Laboratory experiments on fault behavior towards better
615   understanding of injection-induced seismicity in geoenergy systems. *Earth-Science Reviews*, *226*(1),doi:
616   0.1016/j.earscirev.2021.103916.

617 Ji, Y., Fang, Z., & Wu, W. (2021). Fluid Overpressurization of Rock Fractures: Experimental Investigation and
618   Analytical Modeling. *Rock Mechanics and Rock Engineering*, *54*(6318), doi: 10.1007/s00603-021-02453-8.

619 Ji, Y., Wanniarachchi, W.A.M., & Wu, W. (2020). Effect of fluid pressure heterogeneity on injection-induced
620   fracture activation. *Computers and Geotechnics*, *123*(6318), 103589, doi: 10.1016/j.compgeo.2020.103589.

621 Ji, Y., & Wu, W. (2020). Injection-driven fracture instability in granite: Mechanism and implications.
622   *Tectonophysics*, *791*(B12), 228572, doi: 10.1016/j.tecto.2020.228572.

623 Ji, Y. . (2020). *Shear-flow characteristics of rock fractures and implications for injection-induced seismicity*.
624   Ph.D. Nanyang Technological University, doi: 10.32657/10356/143989.

625 Ji, Y. , Wu, W., & Zhao, Z. (2019). Unloading-induced rock fracture activation and maximum seismic moment
626   prediction. *Engineering Geology*, *262*(6), doi: 10.1016/j.enggeo.2019.105352.

627 Jia, Y., Wu, W., & Kong, X.Z. (2020). Injection-induced slip heterogeneity on faults in shale reservoirs.
628   *International Journal of Rock Mechanics and Mining Sciences*, *131*(3), 104363, doi:
629   10.1016/j.ijrmms.2020.104363.

630 Kakurina, M., Guglielmi, Y., Nussbaum, C., & Valley, B. (2019). Slip perturbation during fault reactivation by
631   a fluid injection. *Tectonophysics*, *757*, 140–152, doi: 10.1016/j.tecto.2019.01.017.

632 Keranen, K. M., Savage, H. M., Abers, G. A., & Cochran, E. S. (2013). Potentially induced earthquakes in
633   Oklahoma, USA: Links between wastewater injection and the 2011 Mw 5.7 earthquake sequence. *Geology*,
634   *41*(6), 699-702,doi: 10.1130/G34045.1

635 Kim, K. H., Ree, J. H., Kim, Y. H., Kim, S., Kang, S. Y., & Seo, W. (2018). Assessing whether the 2017 Mw
636   5.4 Pohang earthquake in South Lorea was an induced event. *Science*, *360*(6392), 1007-1009, doi:
637   10.1126/science.aat6081.

638   Lengliné, O., Boubacar, M., & Schmittbuhl, J. (2017). Seismicity related to the hydraulic stimulation of GRT1,
639   Rittershoffen, France. *Geophysical Journal International*, 208(3):ggw490, doi:10.1093/gji/ggw490.

640   Majer, E. L., Baria, R., Stark, M., Oates, S., Bommer, J., & Smith, B., et al. (2007). Induced seismicity associated
641   with enhanced geothermal systems. *Geothermics*, *36*(3), 185-222, doi: 10.1016/j.geothermics.2007.03.003.

642   Maurer, J., & Segall, P., 2018. Magnitudes of Induced Earthquakes in Low-Stress Environments. *Bulletin of the*
643   *Seismological Society of America*, *108*(3), 1087–1106, doi: 10.1785/0120170295.

644   Mclaskey, G. C., & Yamashita, F. (2017). Slow and fast ruptures on a laboratory fault controlled by loading
645   characteristics. *Journal of Geophysical Research: Solid Earth*, *122*(5), doi: 10.1002/2016JB013681.

646   Mohammadioun, B. (2001). Stress Drop, Slip Type, Earthquake Magnitude, and Seismic Hazard. Bull Seismol
647   Soc Amer, *91*(4), 694–707, doi: doi.org/10.1785/0120000067.

648   Palmer, A.C., & Rice, J.R. (1973). The Growth of Slip Surfaces in the Progressive Failure of Over-Consolidated
649   Clay. *Proceedings of The Royal Society a Mathematical Physical and Engineering Sciences*, *332*(1591):527-
650   548, doi: 10.1098/rspa.1973.0040.

651   Passelègue, François.X., Brantut, N., & Mitchell, T.M. (2018). Fault Reactivation by Fluid Injection: Controls
652   From Stress State and Injection Rate. *Geophysical Research Letters*, *45*(23), doi: 10.1029/2018GL080470.

653   Passelègue, François.X., Schubnel, A. , Nielsen, S. , Bhat, H. , Deldicque, D. , & Raùl Madariaga, et al. (2019).
654   Dynamic rupture processes inferred from laboratory microearthquakes. *Journal of Geophysical Research:*
655   *Solid Earth*, 121(6), doi: 10.1002/2015JB012694.

656   Ruina, A. (1983). Slip instability and state variable friction laws. *Journal of Geophysical Research: Solid Earth,*
657   *88*(B12), 10359–10370, doi: 10.1029/JB088iB12p10359.

658   Rutter, E., & Hackston, A. (2017). On the effective stress law for rock-on-rock frictional sliding, and fault slip
659   triggered by means of fluid injection. *Philosophical Transactions of The Royal Society A Mathematical*
660   *Physical and Engineering Sciences*, *375*(2103):20160001, doi: 10.1098/rsta.2016.0001.

661   Scholz, C., Molnar, P., & Johnson, T. (1972). Detailed studies of frictional sliding of granite and implications
662   for the earthquake mechanism. *Journal of Geophysical Research*, *77*(32), 6392-6406, doi:
663   10.1029/JB077i032p06392.

664   Tembe, S. , Lockner, D. A. , & Wong, T. . (2010). Effect of clay content and mineralogy on frictional sliding
665   behavior of simulated gouges: binary and ternary mixtures of quartz, illite, and montmorillonite. *Journal of*
666   *Geophysical Research*: *Solid Earth*, *115*(B3), doi: 10.1029/2009JB006383.Tsutsumi, A., & Shimamoto, T.
667   (1997). High-velocity frictional properties of gabbro. *Geophysical Research Letters*, *24*(6):699-702, doi:
668   10.1029/97GL00503.

669   Ujiie, K., & Tsutsumi, A. (2010). High-velocity frictional properties of clay-rich fault gouge in a megasplay
670   fault zone, Nankai subduction zone. *Geophysical Research Letters*, *37*(24), doi: 10.1029/2010GL046002.

671   van der Elst, N.J., Page, M.T., Weiser, D.A., Goebel, T.H.W., & Hosseini, S.M., 2016. Induced earthquake
672   magnitudes are as large as (statistically) expected: Induced earthquake maximum magnitudes. *Journal of*
673   *Geophysical Research*: *Solid Earth*, *121*(6), 4575–4590, doi: 10.1002/2016JB012818.

674   Vogler, D. , Amann, F. , Bayer, P. , & Elsworth, D. (2016). Permeability evolution in natural fractures subject

675   to cyclic loading and gouge formation. *Rock Mechanics&Rock Engineering* ,*49*(9), doi: 10.1007/s00603-016-

676   1022-0.

677   Wang, L., Kwiatek, G., Rybacki, E., Bonnelye, A., Bohnhoff, M., & Dresen, G. (2020). Laboratory Study on

678   Fluid-Induced Fault Slip Behavior: The Role of Fluid Pressurization Rate. *Geophysical Research Letters*.

679   *47*(6), doi: 10.1029/2019GL086627.

680   Wu, W., Reece, J.S., Gensterblum, Y., & Zoback, M.D. (2017). Permeability Evolution of Slowly Slipping

681   Faults in Shale Reservoirs. *Geophysical Research Letters*, *44*(24), 11368-11375, doi:10.1002/2017gl075506.

682   Ye, Z., & Ghassemi, A. (2018). Injection-Induced Shear Slip and Permeability Enhancement in Granite Fractures.

683   *Journal of Geophysical Research*: *Solid Earth*, *123*, 9009–9032, doi: 10.1029/2018JB016045.

684   Yu F., Arnaud M., Didier S., Ke G.(2022). Investigating Injection Pressure as a Predictor to Enhance Real-Time

685   Forecasting of Fluid-Induced Seismicity: A Bayesian Model Comparison. *Seismological Research Letters*,1-

686   22, doi: https://doi.org/10.1785/0220220309

687   Zhao, Q., Tisato, N., Kovaleva, O., & Grasselli, G.(2018a). Direct Observation of Faulting by Means of Rotary

688   Shear Tests Under X-Ray Micro-Computed Tomography. *Journal of Geophysical Research*: *Solid Earth*,

689   *123*(9),7389–7403, doi: 10.1029/2017JB015394.

690   Zhao, Z., Peng, H., Wu, W., & Chen, Y. F. (2018b). Characteristics of shear-induced asperity degradation of

691   rock fractures and implications for solute retardation. *International Journal of Rock Mechanics and Mining*

692   *Sciences, 105*, 53–61, doi: 10.1016/j.ijrmms.2018.03.012.

693   Zhang, E. et al. (2022). The first power generation test of hot dry rock resources exploration and production

694   demonstration project in the Gonghe Basin, Qinghai Province, China, *China Geology*, 5(3), 372–382,

695   doi:10.31035/cg2022038.